



Single-impurity Anderson model out of equilibrium: A two-particle semianalytic approachJiawei Yan * and Václav Janiš *Institute of Physics of the Czech Academy of Sciences, Na Slovance 1999/2, 182 00 Prague 8, Czech Republic*

(Received 30 September 2021; revised 31 January 2022; accepted 1 February 2022; published 14 February 2022)

We apply a two-particle semianalytic approach to a single Anderson impurity attached to two biased metallic leads. The theory is based on reduced parquet equations justified in critical regions of singularities in the Bethe-Salpeter equations. It offers a way to treat one-particle and two-particle thermodynamic and spectral quantities on the same footing. The two-particle vertices are appropriately renormalized so that spurious transitions into the magnetic state of the weak-coupling approximations are suppressed. The unphysical hysteresis loop in the current-voltage characteristics is thereby eliminated. Furthermore, in the linear response regime, we qualitatively reproduce the three transport regimes with the increasing temperature: from the Kondo resonant tunneling through the Coulomb-blockade regime up to a sequential tunneling regime. Far from equilibrium, we find that the bias plays a similar role as the temperature in destroying the Kondo resonant peak when the corresponding energy scale is comparable with the Kondo temperature. Aside from that, the applied voltage in low bias is shown to develop spectral peaks around the lead chemical potentials as observed in previous theoretical and experimental studies.

DOI: [10.1103/PhysRevB.105.085122](https://doi.org/10.1103/PhysRevB.105.085122)**I. INTRODUCTION**

Finding the full solutions of the single-impurity Anderson model (SIAM) of a magnetic impurity coupled to a metallic reservoir has been an enduring problem in condensed matter physics since the model was first proposed by Anderson [1]. The physics behind this model involves competition between formation of the local magnetic moment in strong coupling and local Fermi liquid in weak coupling at low temperatures. The boundary between the two regimes is characterized by an exponentially small Kondo temperature T_K [2,3].

Despite the simple form of the Anderson Hamiltonian the solution of the SIAM plays a crucial role in the development of modern theoretical methods for strongly correlated systems since (i) it is one of the few many-body quantum problems that is exactly solvable under some specific conditions [4] and (ii) it offers an impurity solver for the dynamical mean-field theory (DMFT) of the Hubbard model [5]. The SIAM then serves as a benchmark on which many-body computational methods are tested. The dynamical mean-field theory built upon the SIAM combined with the density functional theory (DFT) has become one of the most effective ways to implement strong electron correlations into realistic calculations of the electronic structure of solids [6]. Due to wide applicability of the SIAM, generalizations of the standard SIAM have been proposed for modeling quantum dots in different conditions such as (i) impurity with s -wave superconducting leads, representing 0 - π junctions [7], (ii) complex of quantum dots [8], (iii) in the presence of spin-orbit coupling [9], etc. All these impurity problems cannot be solved exactly due to the onsite Coulomb repulsion.

The focus shifted in the last two decades from equilibrium to nonequilibrium situations [10–12]. The problem becomes even more complex and adaptations of the equilibrium methods are necessary. The numerically exact quantum Monte Carlo (QMC) [13,14] sampling Feynman diagrams without bias giving a direct access to thermodynamic quantities at nonzero temperatures, the numerical renormalization group (NRG) [15], the functional renormalization group (fRG) [16,17], as well as the time-dependent density-matrix renormalization group (tDMRG) [18–20] generically based on RG flows towards fixed points reproducing thus well the exact low-temperature spectra, were already extended beyond equilibrium.

It is generally demanding to reach numerically exact solutions even in simple impurity models out of equilibrium. That is why analytic and semianalytic approaches have also been extended to assess nonequilibrium low-temperature behavior of impurity models. Many-body Green functions proved to become the most suitable tools to achieve this goal. They may be treated and approximated in various ways. The equation-of-motion (EOM) scheme truncates the hierarchy of equations for many-body Green function at a certain particle level [12,21]. The standard many-body perturbation theory (MBPT) in the interaction strength with Feynman diagrams is mostly cut in weak coupling at second order [22–24]. Extensions to intermediate coupling in nonequilibrium was achieved by the GW scheme [25] or by the T matrix [26]. A strong-coupling (infinite interaction) approach was also applied out of equilibrium [10]. Besides, quantum master-equation approach truncating the infinite dimension of the leads by a coupling to the bath governed by Lindbladian dynamics was used to simulate nonequilibrium situations [27,28]. Recently, significant efforts have also been made in time-dependent density

*yan@fzu.cz

functional theory (TD-DFT) to the nonequilibrium SIAM, which have potential application for realistic material calculations [29–31]. Nevertheless, none of the standard methods are applicable in all situations, hence, new approximate schemes have been introduced in many-body models in recent years [32–34].

The equilibrium Kondo effect plays an important role in the description of all the transport regimes through a strongly correlated quantum dot. It is hence mandatory for any approximate theory of nonequilibrium phenomena to cover at least qualitatively correctly the Kondo strong-coupling equilibrium regime. Apart from pure numerical simulations it is the Fermi-liquid theory extended to out of equilibrium [35–38]. This approach uses the input from the equilibrium NRG calculations of the correlations-induced enhancements of the Fermi-liquid parameters reaching thereby rather precise description of the low-temperature Kondo regime in the leading order of the voltage bias. Another approach that can qualitatively correctly describe the equilibrium strong-coupling Kondo regime was introduced by one of the present authors [39–43]. It is a mean-field-like theory with a two-particle self-consistency replacing the bare interaction with a screened one. It is based on the parquet construction of the two-particle irreducible vertex and interpolates reliably between weak and strong couplings of impurity and extended lattice models. The approximation is rather simple. It reproduces qualitatively correctly the Kondo regime and it is in overall agreement with more advanced numerical methods in the whole parameter space [42]. Although it cannot predict the Kondo strong-coupling asymptotics with logarithmic corrections numerically as precisely as the Fermi-liquid approach using NRG input, it can be extended, unlike the Fermi-liquid approach, consistently to the whole region of the input parameters of the impurity models, including the voltage bias. Motivated by these facts, we extend here the reduced parquet equations for the two-particle irreducible vertex from Ref. [42] to systems out of equilibrium that will allow us to study transport properties available experimentally [44–46].

The reduced parquet equations in their static approximation introduce a renormalization of the bare interaction suppressing the spurious transition to a magnetically ordered state, the magnetic susceptibility remains positive, and the solution is free of the unphysical hysteresis loop in the current-voltage characteristics of the weak-coupling approximations without a two-particle self-consistency for out-of-equilibrium systems. Additionally, the three-peak structure of the equilibrium spectral function is maintained with the correct logarithmic Kondo scaling of the width of the central quasiparticle peak with the interaction strength. We further reveal three transport stages with the increasing of temperature in the linear response regime of this approximation. They are the Kondo resonant tunneling, the Coulomb-blockade regime, and a sequential tunneling [22,47]. Farther from equilibrium, we find that the biased voltage inducing the nonequilibrium quantum statistics plays a similar role as temperature in equilibrium in that it destroys the Kondo peak when its value is comparable with the Kondo temperature T_K . Aside from that, the bias also develops a local spectral peak around the chemical potential of each lead [10,44]. These local peaks

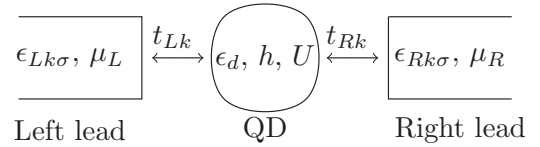


FIG. 1. Sketch of the transport model, whose Hamiltonian is given by Eq.(1).

vanish quickly with the increase of the voltage and finally become unrecognizable.

The paper is organized as follows. We introduce the model Hamiltonian as well as the Keldysh-Schwinger nonequilibrium Green function (NEGF) perturbation theory in Sec. II. The two-particle approach with the reduced parquet equations formulated in the Keldysh space is introduced in Sec. III. The real-time formulation to study the steady-state quantum transport problem is presented in Sec. IV. Results are discussed in Sec. V followed by the concluding Sec. VI. Important technical details of the derivations are moved to the Appendices.

II. MODEL HAMILTONIAN AND NEGF THEORY

A. Generic model Hamiltonian

We describe a single quantum dot (QD) attached to two biased semi-infinite metallic leads, as shown in Fig. 1, by the following Hamiltonian:

$$H = \sum_s (H_s^{\text{ld}} + H_s^{\text{hyb}}) + H^{\text{dot}}, \quad s \in \{L, R\} \quad (1)$$

where H_s^{ld} , H^{dot} , and H_s^{hyb} correspond respectively to the Hamiltonian of the s lead, the QD, and the hybridization between them. The explicit forms of the partial Hamiltonians are

$$H_s^{\text{ld}} = \sum_{k\sigma} (\epsilon_{sk\sigma} - \mu_s) c_{sk\sigma}^\dagger c_{sk\sigma}, \quad (2)$$

$$H_s^{\text{hyb}} = - \sum_{k\sigma} (t_{sk} d_\sigma^\dagger c_{sk\sigma} + t_{sk}^* c_{sk\sigma}^\dagger d_\sigma), \quad (3)$$

$$H^{\text{dot}} = \sum_\sigma (\epsilon_d - \sigma h) d_\sigma^\dagger d_\sigma + U d_\uparrow^\dagger d_\uparrow d_\downarrow^\dagger d_\downarrow \quad (4)$$

with $c_{sk\sigma}^{(\dagger)}$ and $d_\sigma^{(\dagger)}$ the annihilation (creation) operators of the lead and QD electrons, respectively. We denoted $\epsilon_{sk\sigma}$ the dispersion relation of the lead electrons, μ_s is the chemical potential of the s lead, and ϵ_d is the atomic level of the QD. The Zeeman magnetic field h splits the spin orientation $\sigma = \pm 1$ corresponding to up and down spin projection. The hybridization between the QD and the s lead is t_{sk} and U is the charging energy on the QD. The left and right semi-infinite leads are assumed to be in local equilibrium and their chemical potentials are equal, $\mu_L = \mu_R = \mu$, in the absence of the bias voltage. They are shifted by a factor qV when applying a bias voltage $V > 0$, as $\mu_L = \mu - qV/2$ and $\mu_R = \mu + qV/2$, where $q = -e$ ($e > 0$) is the unity charge of an electron. Therefore, the electrons always flow from left to the right. Hereinafter, natural units are taken, i.e., $e = 1$, $\hbar = 1$.

B. Many-body perturbation expansion

The Hamiltonian in Eq. (1) cannot be straightforwardly diagonalized and neither equilibrium nor nonequilibrium properties can be obtained exactly in a full extent. We hence use the many-body perturbation theory with Green functions extended to nonequilibrium situations within the Schwinger-Keldysh formalism. Instead of the linear one-way time ordering of equilibrium we have to introduce an ordering along a Keldysh contour \mathbb{C} in the plane of complex times consisting generally from three branches out of equilibrium [24,48].

Since we are interested only in the physics on the dot, the nonlocal degrees of freedom of the leads can be projected (integrated) out and to a problem with only local dynamical degrees of freedom. We define the local Keldysh contour-ordered Green function on the quantum dot as

$$G_{\sigma}(z, z') = -i\langle T_{\mathbb{C}}\{d_{\sigma}(z), d_{\sigma}^{\dagger}(z')\}\rangle, \quad (5)$$

where the thermal average of operator O is given by $\langle O \rangle = \text{Tr}[\rho O]$, where ρ is the equilibrium density operator at an initial time t_i . Further, $d_{\sigma}(z)$ and $d_{\sigma}^{\dagger}(z')$ are the operators in the Heisenberg picture evolving along the Keldysh contour \mathbb{C} . The first forward branch of the Keldysh contour goes from t_i to t_f , the second one returns back from t_f to t_i , and the third one is purely imaginary from t_i to $t_i - i\beta$. We used a symbol $T_{\mathbb{C}}$ for the contour-ordering operator which put the operators along the contour in the ascending order according to complex time $z \in \mathbb{C}$.

Although we will derive the formulas in the general Keldysh formalism, we will finally be interested only in long times with $t_i \rightarrow -\infty$ and the Hubbard interaction U switched on adiabatically. The initial state at t_i has then only little impact on the observed time evolution. We can hence cut off the imaginary leg of the Keldysh contour and replace it with thermal averaging with the noninteracting Hamiltonian [23,24,49–51]. The Green function from Eq. (5) can then be represented as

$$G_{\sigma}(z, z') = -i\langle T_{\supset}\{d_{\sigma}(z), d_{\sigma}^{\dagger}(z')\}\rangle, \quad (6)$$

where the angular brackets denote now the thermodynamic averaging with the noninteracting Hamiltonian and the T_{\supset} is the time ordering along the two-leg Keldysh real-time contour. One can derive various real-time Green functions from the contour-ordered one $G_{\sigma}(z, z')$, depending on which branch the time arguments z and z' reside (see Appendix A).

We first resolve the nonequilibrium Green function from Eq. (6) for the noninteracting dot, that is, for $U = 0$, exactly. Their impact on the physics of the dot reduces to a hybridization self-energy $\Sigma_{\sigma}^{\text{ld}}(z, z') = \sum_{s \in L, R} \Sigma_{s\sigma}^{\text{ld}}(z, z')$ after integrating their degrees of freedom. We further use a wide-band limit (WBL) where the density of states of the lead electrons is approximated by its value at the chemical potential [52]. This approximation works well if the density of states of the leads only slowly varies around the Fermi level (see Appendix B).

The hybridization self-energy from the leads enters the following left and right Dyson equations for

the two time variables of the nonequilibrium Green function [23,24]

$$\begin{aligned} & \left(+i\frac{\overrightarrow{d}}{dz} - \epsilon_d + \sigma h \right) G_{\sigma}^0(z, z') \\ & = \delta(z - z') + \int_{\supset} d\bar{z} \Sigma_{\sigma}^{\text{ld}}(z, \bar{z}) G_{\sigma}^0(\bar{z}, z'), \end{aligned} \quad (7a)$$

$$\begin{aligned} & G_{\sigma}^0(z, z') \left(-i\frac{\overleftarrow{d}}{dz'} - \epsilon_d + \sigma h \right) \\ & = \delta(z - z') + \int_{\supset} d\bar{z} G_{\sigma}^0(z, \bar{z}) \Sigma_{\sigma}^{\text{ld}}(\bar{z}, z'). \end{aligned} \quad (7b)$$

Notice that $\delta(z - z')$ is a contour delta function so that $\int_{\mathbb{C}} dz \delta(z - z') = 1$. It means that $\delta(-i(\tau - \tau')) = i\delta(\tau - \tau')$ for $\tau, \tau' \in (0, \beta)$ on the imaginary leg of the Keldysh contour.

The impact of the Coulomb interaction is contained in the interaction self-energy $\Sigma_{\sigma}^{\text{int}}(z, z')$ that will be determined from the many-body perturbation theory [22–24]. The interaction self-energy $\Sigma_{\sigma}^{\text{int}}(z, z')$ determines the full nonequilibrium Green function from Eq. (6) via Dyson integral equation

$$\begin{aligned} G_{\sigma}(z, z') & = G_{\sigma}^0(z, z') + \int_{\supset} dz_1 dz_2 G_{\sigma}^0(z, z_1) \\ & \quad \times \Sigma_{\sigma}^{\text{int}}(z_1, z_2) G_{\sigma}(z_2, z'). \end{aligned} \quad (8)$$

The interacting self-energy should be calculated from the renormalized perturbation expansion in the interaction strength. A consistent scheme for introducing renormalizations in the equilibrium perturbation theory was introduced by Baym and Kadanoff [53–55]. This scheme was later extended to nonequilibrium quantum transport [23–25]. The interacting self-energy is directly related to the two-particle vertex $\Gamma_{\sigma\bar{\sigma}}$ in the Baym-Kadanoff approach via the Schwinger-Dyson equation. Its nonequilibrium form for the quantum dot is

$$\begin{aligned} \Sigma_{\sigma}^{\text{int}}(z, z') & = U n_{\bar{\sigma}}(z) \delta(z - z') \\ & \quad - iU \int_{\supset} dz_1 dz_2 dz_4 G_{\sigma}(z, z_1) \Gamma_{\sigma\bar{\sigma}}(z_1, z_2, z', z_4) \\ & \quad \times G_{\bar{\sigma}}(z_4, z) G_{\bar{\sigma}}(z, z_2), \end{aligned} \quad (9)$$

where $\bar{\sigma} = -\sigma$.

The self-energy is the irreducible part of the one-electron propagator. We can also introduce a two-particle irreducible vertex from which the full vertex is obtained via a Bethe-Salpeter equation in analogy with the Dyson equation. Unlike the one-particle irreducibility, the two-particle irreducibility is not uniquely defined [56–59]. If we choose the electron-hole irreducibility and introduce the electron-hole irreducible vertex Λ^{eh} , the nonequilibrium Bethe-Salpeter equation for the two-particle vertex reads as

$$\begin{aligned} \Gamma_{\sigma\bar{\sigma}}(z_1, z_2, z_3, z_4) & = \Lambda_{\sigma\bar{\sigma}}^{eh}(z_1, z_2, z_3, z_4) \\ & \quad + \int_{\supset} dz_1 dz_2 dz_3 dz_4 \Gamma_{\sigma\bar{\sigma}}(z_1, z_2, z_3, z_4) \\ & \quad \times G_{\sigma}(z_3, z_1) G_{\bar{\sigma}}(z_4, z_2) \Lambda_{\sigma\bar{\sigma}}^{eh}(z_1, z_2, z_3, z_4). \end{aligned} \quad (10)$$

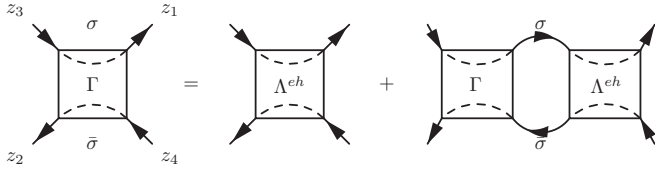


FIG. 2. Diagrammatic representation of the Bethe-Salpeter equation in the electron-hole channel with the notation of the vertex and the spin variables.

Its diagrammatic representation is plotted in Fig. 2.

The two-particle irreducible vertices are not the integral part of the Baym-Kadanoff approach where only one-particle functions are used. They are, however, important for checking whether the solution with the two-particle vertex Γ from the Schwinger-Dyson equation (9) and obeying the Bethe-Salpeter equation (10) is conserving. It is the case if the self-energy Σ and the two-particle irreducible vertex Λ^{eh} obey a functional Ward identity [54] that in our notation and the selection of the variables of the two-particle vertex (see Fig. 2) reads as

$$\Lambda_{\sigma\bar{\sigma}}^{eh}(z_1, z_2, z_3, z_4) = -\frac{\delta\Sigma_{\sigma}(z_1, z_3)}{\delta G_{\bar{\sigma}}(z_4, z_2)}. \quad (11)$$

It was shown, however, that no approximate solution can obey simultaneously the Schwinger-Dyson equation and the Ward identity with a single self-energy and a single two-particle vertex [42,57]. We show in the next section how to qualitatively reconcile the Ward identity and the Schwinger-Dyson equation.

III. TWO-PARTICLE SELF-CONSISTENCY

A. Generating two-particle vertex and self-energies

The Baym-Kadanoff approach is based on the existence of a generating Luttinger-Ward functional $\Phi[G, U]$ from which all quantities are derived via functional derivatives with respect to G . The first derivative of this functional leads to the Schwinger-Dyson equation for the self-energy that is uniquely defined. Its second derivatives lead to two-particle irreducible vertices. Since we cannot obey Ward identity (11) and the Schwinger-Dyson equation (9) simultaneously in any approximation with a single self-energy, two-particle vertices are then defined ambiguously. It does not matter much if the difference between the two-particle vertices from the Schwinger-Dyson equation and from the Bethe-Salpeter equation with the irreducible vertex from the Ward identity is only quantitative. We come into trouble, however, if we approach a critical point of a continuous phase transition. The phase transition remains continuous only if the Ward identity is obeyed at least in the linear order of the symmetry-breaking field, conjugate to the order parameter. The uniqueness of the critical behavior demands the existence of a unique two-particle vertex. That is why one of the authors proposed an alternative construction of the renormalized perturbation expansion. The basic idea of this construction is to use the two-particle irreducible vertex from the critical Bethe-Salpeter equation as the generating functional of the perturbation theory [39–43].

This construction can be straightforwardly extended beyond equilibrium.

We assume here that the potential critical behavior is a transition to a magnetically ordered phase with the order parameter conjugate to the magnetic field. The potentially divergent Bethe-Salpeter equation in equilibrium is that with multiple electron-hole scatterings, Eq. (10). We hence choose $\Lambda_{\uparrow\downarrow}^{eh}$ as the generating functional. It is sufficient to resolve the Ward identity only in the linear order in the magnetic field to maintain consistency between the order parameter and the singular two-particle vertex. To do so, we separate one-particle functions to those with odd and even symmetry with respect to the magnetic field. We denote

$$\Delta G(z, z') = \frac{1}{2}[G_{\sigma}(z, z') - G_{\bar{\sigma}}(z, z')], \quad (12a)$$

$$\bar{G}(z, z') = \frac{1}{2}[G_{\sigma}(z, z') + G_{\bar{\sigma}}(z, z')]. \quad (12b)$$

The self-energy resolved from Ward identity (11) for a given two-particle irreducible vertex Λ^{eh} has odd symmetry and in the the linear order it reads as

$$\Delta\Sigma^{\text{int}}(z_1, z_3) = \int_{\triangleright} dz_2 dz_4 \Lambda_s^{eh}(z_1, z_2, z_3, z_4) \Delta G(z_4, z_2), \quad (13)$$

where $\Lambda_s^{eh} = (\Lambda_{\downarrow\uparrow}^{eh} + \Lambda_{\uparrow\downarrow}^{eh})/2$ is the symmetric spin-singlet electron-hole irreducible vertex. We do not need to consider odd two-particle functions since the order parameter of the ordered phase is a one-particle quantity.

The Ward identity affects only the odd self-energy being nonzero only in the ordered phase. The even self-energy is untouched by the Ward identity and is determined separately from the Schwinger-Dyson equation. We must, however, use the symmetrized one-particle propagator \bar{G} not to change the thermodynamic consistency, that is, the critical behavior of the vertex from the Schwinger-Dyson equation is that determined from the derivative of the odd self-energy. The Schwinger-Dyson equation (9) changes to

$$\begin{aligned} \bar{\Sigma}^{\text{int}}(z, z') &= \frac{U}{2}n(z)\delta(z - z') \\ &- iU \int_{\triangleright} dz_1 dz_2 dz_4 \bar{G}(z, z_1) \Gamma_s(z_1, z_2, z', z_4) \\ &\times \bar{G}(z_4, z) \bar{G}(z, z_2), \end{aligned} \quad (14)$$

where $n(z) = n_{\uparrow}(z) + n_{\downarrow}(z)$ is the total charge density and the Bethe-Salpeter equation (10) changes to

$$\begin{aligned} \Gamma_s(z_1, z_2, z_3, z_4) &= \Lambda_s^{eh}(z_1, z_2, z_3, z_4) + \int_{\triangleright} dz_1 dz_2 dz_3 dz_4 \\ &\times \Gamma_s(z_1, z_2, z_3, z_4) \bar{G}(z_3, z_1) \\ &\times \bar{G}(z_4, z_2) \Lambda_s^{eh}(z_1, z_2, z_3, z_4). \end{aligned} \quad (15)$$

The full interaction spin-dependent self-energy is then a sum of the even and the odd self-energies, that is [42],

$$\Sigma_{\sigma}^{\text{int}}(z, z') = \bar{\Sigma}^{\text{int}}(z, z') + \sigma \Delta\Sigma^{\text{int}}(z, z'). \quad (16)$$

The unique two-particle vertex determines the self-energy that obeys the Ward identity in the linear order of the symmetry-breaking field and thereby guarantees that the order parameter

develops continuously from zero below the critical point of the phase transition to a magnetically ordered phase.

B. Reduced parquet equations

The two-particle approach guarantees thermodynamic qualitative consistency between the susceptibility and the order parameter. The quality of the approximation depends on the selection of the symmetric singlet electron-hole irreducible vertex Λ_s^{eh} . If we choose the simplest approximation $\Lambda_s^{eh}(z_1, z_2, z_3, z_4) = iU\delta(z_1 - z_2)\delta(z_2 - z_3)\delta(z_3 - z_4)$, then the symmetric self-energy leads either to FLEX or RPA spin-symmetric solutions in the high-temperature phase, depending on whether the one-particle propagators are renormalized or not. These approximations fail in the strong-coupling limit and an improved two-particle vertex should be selected. We introduce a two-particle self-consistency to suppress the spurious transition to the magnetic state of the weak-coupling approximations. The most straightforward way to introduce a two-particle self-consistency is to use the parquet construction of the two-particle vertex.

It is sufficient to use only two Bethe-Salpeter equations to provide a reliable transition from weak to strong coupling. We choose the Bethe-Salpeter equation in the electron-hole (eh) channel in this case which becomes singular at the magnetic transition. The other equation must attenuate the tendency towards the critical point. It is the Bethe-Salpeter equation in the electron-electron (ee) channel for the magnetic transition. Its symmetric version out of equilibrium reads as

$$\begin{aligned} \Gamma_s(z_1, z_2, z_3, z_4) &= \Lambda_s^{ee}(z_1, z_2, z_3, z_4) \\ &+ \int_{\mathcal{D}} dz_1 dz_2 dz_3 dz_4 \Lambda_s^{ee}(z_1, z_2, z_3, z_4) \\ &\times \bar{G}(z_3, z_1) \bar{G}(z_4, z_2) \Gamma_s(z_1, z_2, z_3, z_4). \end{aligned} \quad (17)$$

The fundamental idea of the parquet approach is to use the fact that the reducible diagrams in one channel are irreducible in the other scattering channels. We denote \mathcal{K}^α the reducible vertex in channel α , that is $\Gamma = \Lambda^\alpha + \mathcal{K}^\alpha$. The fundamental parquet equation in the two-channel scheme can be written in either of the following two forms:

$$\Gamma_s(z_1, z_2, z_3, z_4) = \Lambda_s^{eh}(z_1, z_2, z_3, z_4) + \Lambda_s^{ee}(z_1, z_2, z_3, z_4) - I_s(z_1, z_2, z_3, z_4), \quad (18a)$$

$$\Gamma_s(z_1, z_2, z_3, z_4) = \mathcal{K}_s^{eh}(z_1, z_2, z_3, z_4) + \mathcal{K}_s^{ee}(z_1, z_2, z_3, z_4) + I_s(z_1, z_2, z_3, z_4). \quad (18b)$$

We introduced the fully two-particle irreducible vertex $I_s(z_1, z_2, z_3, z_4)$ that becomes the generator of the perturbation theory in the parquet approach. Using one of these representations of the full two-particle vertex in the Bethe-Salpeter equations (15) and (17) we obtain a set of coupled equations determining self-consistently either irreducible Λ_s^{eh} , Λ_s^{ee} or reducible \mathcal{K}_s^{eh} , \mathcal{K}_s^{ee} vertices.

The full solution of the parquet equations with $I_s(z_1, z_2, z_3, z_4) = iU\delta(z_1 - z_2)\delta(z_2 - z_3)\delta(z_3 - z_4)$ and with two or three channels, suppresses the critical behavior [60]. One has either to go beyond the bare interaction for the fully irreducible vertex or one can modify the parquet equations so

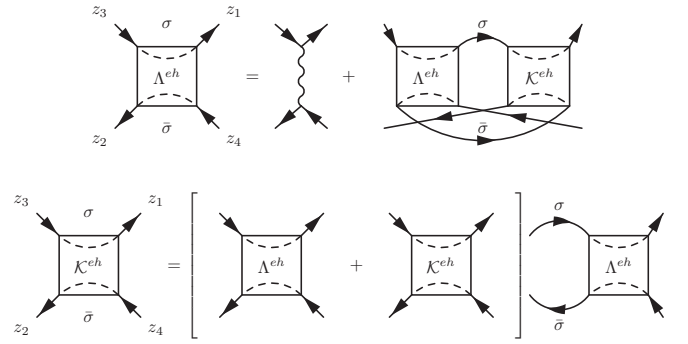


FIG. 3. Diagrammatic representation of the reduced Parquet equations in electron-electron (first row) and electron-hole channels (second row). The vertex diagrams in the brackets are connected to the left propagators by the appropriate multiplication rules.

that the critical behavior of the weak-coupling approximations is not completely destroyed. One of the authors proposed to get rid of the terms in the parquet equations that suppress the critical behavior in the electron-hole channel and replaced the full set of the two-channel parquet equations with a couple of the so-called reduced parquet equations [42]. The equation for the regular irreducible vertex in the electron-hole channel is then reduced to

$$\begin{aligned} \Lambda_s^{eh}(z_1, z_2, z_3, z_4) &= iU\delta(z_1 - z_3)\delta(z_2 - z_4)\delta(z_1 - z_4) \\ &+ \int_{\mathcal{D}} dz_1 dz_2 dz_3 dz_4 \Lambda_s^{eh}(z_1, z_2, z_3, z_4) \\ &\times \bar{G}(z_3, z_1) \bar{G}(z_4, z_2) \mathcal{K}_s^{eh}(z_1, z_2, z_3, z_4). \end{aligned} \quad (19)$$

The equation for the reducible vertex in the electron-hole channel remains unchanged:

$$\begin{aligned} \mathcal{K}_s^{eh}(z_1, z_2, z_3, z_4) &= \int_{\mathcal{D}} dz_1 dz_2 dz_3 dz_4 \\ &\times [\mathcal{K}_s^{eh}(z_1, z_2, z_3, z_4) \\ &+ \Lambda_s^{eh}(z_1, z_2, z_3, z_4)] \bar{G}(z_3, z_1) \\ &\times \bar{G}(z_4, z_2) \Lambda_s^{eh}(z_1, z_2, z_3, z_4). \end{aligned} \quad (20)$$

The diagrammatic representation of these equations is given in Fig. 3. We showed that the reduced parquet equations correctly reproduce the Kondo regime of SIAM at equilibrium [3,40,42].

C. Instantaneous effective interaction

The reduced parquet equations do not simplify the complexity of the full set of parquet equations. They cannot be solved easily due to the unrestricted four-time dependence of the two-particle vertices. To simplify the problem, we resort to an instantaneous effective interaction or the local time approximation (LTA), which assumes that the irreducible vertex $\Lambda_s^{eh}(z_1, z_2, z_3, z_4)$ reduces to an instantaneous effective interaction $i\tilde{\Lambda}_s^{eh}(z_4)\delta(z_1 - z_3)\delta(z_2 - z_4)\delta(z_1 - z_4)$. The reducible vertex $\mathcal{K}_s^{eh}(z_1, z_2, z_3, z_4)$ thus is partially diagonalized, having nonzero values only when $z_1 = z_4$ and $z_2 = z_3$,

thus, one can define $\mathcal{K}_s^{eh}(z_1, z_2, z_3, z_4) = i\tilde{\mathcal{K}}_s^{eh}(z_1, z_2)\delta(z_1 - z_4)\delta(z_2 - z_3)$. As a result, the reduced parquet equations (19) and (20) simplify to

$$\begin{aligned} & [\tilde{\Lambda}_s^{eh}(z_4) - U]\delta(z_1 - z_4)\delta(z_2 - z_4) \\ & = i\tilde{\Lambda}_s^{eh}(z_4)\tilde{\mathcal{K}}_s^{eh}(z_1, z_2)\tilde{G}(z_2, z_4)\tilde{G}(z_1, z_4), \end{aligned} \quad (21)$$

$$\begin{aligned} -[\tilde{\Lambda}_s^{eh}(z_4)]^2\phi_s(z_1, z_2) & = \tilde{\mathcal{K}}_s^{eh}(z_1, z_2) + \tilde{\Lambda}_s^{eh}(z_4) \\ & \times \int_{\square} dz_{\bar{4}}\phi_s(z_1, z_{\bar{4}})\tilde{\mathcal{K}}_s^{eh}(z_{\bar{4}}, z_2), \end{aligned} \quad (22)$$

where we introduced the singlet electron-hole bubble

$$\phi_s(z_1, z_2) = -i\tilde{G}(z_1, z_2)\tilde{G}(z_2, z_1). \quad (23)$$

Equation (22) can be resolved for the reducible vertex $\tilde{\mathcal{K}}_s^{eh}(z_1, z_2)$. If we insert its solution into Eq. (21) its right-hand side maintains a nontrivial dependence on complex times z_1 and z_2 . Since the left-hand side does not depend on z_1, z_2 , we have to resign on point-wise equality in Eq. (21) when the irreducible vertex is approximated via an instantaneous effective interaction. Instead, we replace then Eq. (21) with an equality where both sides are averaged over the redundant time variables. Various averaging schemes can be applied (see [42,61,62]). Different schemes only quantitatively affect the physical behavior far away from the critical region but do qualitatively change the critical behavior itself. Here we multiply both sides of Eq. (21) by $\tilde{G}(z_4, z_2^+)\tilde{G}(z_4, z_1^+)$ and integrate over the redundant time variables z_1 and z_2 . Notice that $z^+ = z + 0^+$ indicates an infinitesimally positive time shift of the variable z . As a result, $\tilde{\Lambda}_s^{eh}$ can be consistently determined from the following alternative (mean-field) equation

$$\tilde{\Lambda}_s^{eh}(z) = \frac{Un(z)n(z)}{n(z)n(z) - 4R_s^{eh}(z)}, \quad (24)$$

with the screening integral

$$R_s^{eh}(z) = i \int_{\square} dz_1 dz_2 \phi_s(z, z_1)\tilde{\mathcal{K}}_s^{eh}(z_1, z_2)\phi_s(z_2, z). \quad (25)$$

Equations (22), (24), and (25) form a closed set determining the two-particle vertices within local-time approximation.

The symmetric two-particle vertex simplifies to $\tilde{\Gamma}_s(z_1, z_2, z_3, z_4) = i\tilde{\Gamma}_s(z_1, z_2)\delta(z_1 - z_4)\delta(z_2 - z_3)$ where $\tilde{\Gamma}_s(z_1, z_2) = \tilde{\mathcal{K}}_s(z_1, z_2) + \tilde{\Lambda}_s^{eh}(z_1)\delta(z_1 - z_2)$. As result, Schwinger-Dyson equation (14) turns to

$$\begin{aligned} \tilde{\Sigma}^{\text{int}}(z, z') & = \frac{U}{2}n(z)\delta(z - z') \\ & + iU\tilde{G}(z, z') \int_{\square} d\bar{z}\phi_s(z, \bar{z})\tilde{\Gamma}_s(\bar{z}, z'), \end{aligned} \quad (26)$$

and the Ward identity (13) becomes

$$\Delta\Sigma(z, z') = i\tilde{\Lambda}_s^{eh}(z)\Delta G(z, z^+)\delta(z - z'). \quad (27)$$

Notice that the electron-hole bubble satisfies a symmetry relation $\phi_s(z_1, z_2) = \phi_s(z_2, z_1)$ and, consequently, $\tilde{\mathcal{K}}_s^{eh}(z_1, z_2) = \tilde{\mathcal{K}}_s^{eh}(z_2, z_1)$ and $\tilde{\Gamma}_s(z_1, z_2) = \tilde{\Gamma}_s(z_2, z_1)$. We drop the superscript “ eh ” and subscript “ s ” in the following sections, since both irreducible and reducible vertices are from the same channel.

IV. STEADY-STATE QUANTUM TRANSPORT

We now apply our two-particle construction with the reduced parquet equations and the instantaneous interaction to the steady-state quantum transport where the system is assumed to be evolved for a sufficiently long time in which it reaches a steady state with time-independent densities and currents [23].

A. Real-time steady-state formalism

The steady-state equations formulated on the Keldysh contour with complex times can be transformed to real times via Langreth rules [23]. We can then use a Fourier transform from time to real frequencies making the defining equations out of equilibrium close to those from equilibrium. Equation (24) becomes time independent,

$$\tilde{\Lambda} = \frac{Un^2}{n^2 - 4R}, \quad (28)$$

since the irreducible vertex and the electron density become time independent in the steady-state case. The screening integral in Eq. (28) is (we refer to Appendix C for details)

$$\begin{aligned} R & = -\frac{1}{4\pi} \int_{-\infty}^{\infty} dx \text{Im}\{[\phi^<(x) + \phi^>(x)]\tilde{\mathcal{K}}^a(x)\phi^a(x) \\ & + \phi^r(x)[\tilde{\mathcal{K}}^<(x) + \tilde{\mathcal{K}}^>(x)]\phi^a(x) \\ & + \phi^r(x)\tilde{\mathcal{K}}^r(x)[\phi^<(x) + \phi^>(x)]\}, \end{aligned} \quad (29)$$

where superscripts $r, a, <, >$ denote the retarded, advanced, lesser, and greater counterparts of the real-time quantities, respectively (see Appendix A). Note that in deriving Eq. (29), we used the fact that R is a real number since $[X^r(w)]^* = X^a(w)$ and $[X^k(w)]^* = -X^k(w)$ where $X \in \{\phi, \tilde{\mathcal{K}}\}$. Additionally, $X^{r/a}(x) = X^{a/r}(-x)$ and $X^{\lessgtr}(x) = X^{\gtrless}(-x)$. Explicitly, we have from Eq. (23)

$$\begin{aligned} \phi^{r/a}(w) & = \frac{-i}{2\pi} \int_{-\infty}^{\infty} dx [\tilde{G}^<(x)\tilde{G}^{a/r}(x-w) \\ & + \tilde{G}^{r/a}(x)\tilde{G}^<(x-w)], \end{aligned} \quad (30a)$$

$$\phi^{\lessgtr}(w) = \frac{-i}{2\pi} \int_{-\infty}^{\infty} dx \tilde{G}^{\lessgtr}(x)\tilde{G}^{\gtrless}(x-w). \quad (30b)$$

We further obtain from Eq. (22)

$$\tilde{\mathcal{K}}^{r/a}(w) + \tilde{\Lambda} = \frac{\tilde{\Lambda}}{1 + \tilde{\Lambda}\phi^{r/a}(w)}, \quad (31a)$$

$$\tilde{\mathcal{K}}^{\lessgtr}(w) = -[\tilde{\Lambda} + \tilde{\mathcal{K}}^r(w)]\phi^{\lessgtr}(w)[\tilde{\Lambda} + \tilde{\mathcal{K}}^a(w)]. \quad (31b)$$

With the above equations, one can self-consistently calculate the two-particle vertices with the given one-particle Green functions.

Once the two-particle vertices are determined, the even and odd parts of the self-energies can be calculated from the Schwinger-Dyson equation and Ward identity, respectively. In particular, the real-time even self-energies read as $\tilde{\Sigma}^{\text{int},r/a}(w) = Un/2 + \tilde{\Sigma}^{\text{cor},r/a}(w)$ and $\tilde{\Sigma}^{\text{int},\lessgtr}(w) = \tilde{\Sigma}^{\text{cor},\lessgtr}(w)$, where, from Eq. (26), we have

$$\bar{\Sigma}^{\text{cor},r/a}(w) = \frac{iU\tilde{\Lambda}}{4\pi} \int_{-\infty}^{\infty} dx \frac{\bar{G}^{r/a}(x)[\phi^<(w-x) + \phi^>(w-x)] + [\bar{G}^<(x) + \bar{G}^>(x)]\phi^{r/a}(w-x)[1 + \tilde{\Lambda}\phi^{a/r}(w-x)]}{[1 + \tilde{\Lambda}\phi^r(w-x)][1 + \tilde{\Lambda}\phi^a(w-x)]}, \quad (32a)$$

$$\bar{\Sigma}^{\text{cor},\leq}(w) = \frac{iU\tilde{\Lambda}}{2\pi} \int_{-\infty}^{\infty} dx \frac{\bar{G}^{\leq}(x)\phi^{\leq}(w-x)}{[1 + \tilde{\Lambda}\phi^r(w-x)][1 + \tilde{\Lambda}\phi^a(w-x)]}. \quad (32b)$$

The real-time odd self-energies, from Eq. (27), become

$$\Delta\Sigma^{\text{int},r/a}(w) = \frac{i\tilde{\Lambda}}{2\pi} \int_{-\infty}^{\infty} dx \Delta G^<(x) = -\frac{m}{2}\tilde{\Lambda}, \quad (33a)$$

$$\Delta\Sigma^{\text{int},\leq}(w) = 0. \quad (33b)$$

The total self-energies are given by $\Sigma_{\sigma}^{\text{int},x}(w) = \bar{\Sigma}^{\text{int},x}(w) + \sigma\Delta\Sigma^{\text{int},x}(w)$ where $x = r, a, >, <$. The spin-dependent renormalized one-particle Green functions are

$$G_{\sigma}^{r/a}(w) = \frac{1}{w + \sigma h_{\Lambda} - \epsilon_U - \Sigma_{\sigma}^{\text{ld},r/a}(w) - \bar{\Sigma}^{\text{cor},r/a}(w)}, \quad (34a)$$

$$G_{\sigma}^{\leq}(w) = G_{\sigma}^r(w)[\Sigma_{\sigma}^{\text{ld},\leq}(w) + \bar{\Sigma}^{\text{cor},\leq}(w)]G_{\sigma}^a(w), \quad (34b)$$

where $\epsilon_U = \epsilon_d + Un/2$, $h_{\Lambda} = h + \tilde{\Lambda}m/2$. The second equation is also well known as the Keldysh formula [23].¹

The renormalized spin-dependent propagator determines the physical quantities. For example, the spin-resolved electron density reads as

$$n_{\sigma} = -\frac{i}{2\pi} \int_{-\infty}^{\infty} G_{\sigma}^<(x)dx. \quad (35)$$

The total electron density and the magnetization are then given by $n = n_{\uparrow} + n_{\downarrow}$ and $m = n_{\uparrow} - n_{\downarrow}$. The spin-resolved current going through s lead is given by [23]

$$J_{s\sigma} = \frac{q}{2\pi} \int_{-\infty}^{\infty} dw [\Sigma_{s\sigma}^{\text{ld},>}(w)G_{\sigma}^<(w) - \Sigma_{s\sigma}^{\text{ld},<}(w)G_{\sigma}^>(w)]. \quad (36)$$

B. Thermodynamic and spectral calculations

The two-particle scheme contains two sets of self-consistent equations. One set is used to determine the two-particle vertex, or the effective interaction. The other set is used to determine the self-energies from the two-particle vertex. One-particle propagators are used in both sets. They are an input in the parquet equations. The vertex function from the parquet equations determines the thermodynamic response and controls the critical behavior of the equilibrium solution. The only consistency condition between the one-particle propagators and the two-particle vertex there is that the odd self-energy of the propagators is determined from the irreducible vertex via the Ward identity. There is no restriction on the even self-energy in the parquet equations. We can hence

¹We neglected the bound-state contributions which are irrelevant to the steady-state transport.

separate the one- and two-particle self-consistencies. We introduce thermodynamic Green functions when we use only the static (HF mean-field) even self-energy in the one-particle propagators determining the two-particle vertex. We will call the Green functions with the full even self-energy from the Schwinger-Dyson equation spectral propagators.

Hereinafter, we denote the quantities calculated with thermodynamic (spectral) calculation by superscript T (S), respectively. The thermodynamic Green functions are

$$G_{\sigma}^{T,r/a}(w) = \frac{1}{w + \sigma h_{\Lambda}^T - \epsilon_U^T - \Sigma_{\sigma}^{\text{ld},r/a}(w)}, \quad (37a)$$

$$G_{\sigma}^{T,\leq}(w) = G_{\sigma}^{T,r}(w)\Sigma_{\sigma}^{\text{ld},\leq}(w)G_{\sigma}^{T,a}(w), \quad (37b)$$

where $h_{\Lambda}^T = h + \tilde{\Lambda}m^T/2$ and $\epsilon_U^T = \epsilon_d + Un^T/2$. Here, n^T and m^T are calculated from the spin-resolved thermodynamic Green functions. Furthermore, the thermodynamic susceptibility can be derived by taking the derivative with respect to the magnetic field

$$\chi^T = \frac{-\sum_{\sigma} \phi_{\sigma\sigma}^{T,r}(0)}{1 + \frac{1}{2}\tilde{\Lambda}\sum_{\sigma} \phi_{\sigma\sigma}^{T,r}(0)}, \quad (38)$$

where

$$\phi_{\sigma\sigma}^{T,r}(0) = \frac{-i}{2\pi} \int_{-\infty}^{\infty} dx [G_{\sigma}^{T,<}(x)G_{\sigma}^{T,a}(x) + G_{\sigma}^{T,r}(x)G_{\sigma}^{T,<}(x)]. \quad (39)$$

The one-particle quantities reduce to the Hartree ones.

The dynamical corrections are added after determining the two-particle vertex via the spectral symmetric self-energy from the Schwinger-Dyson equation. The spectral Green functions read as

$$G_{\sigma}^{S,r/a}(w) = \frac{1}{w + \sigma h_{\Lambda}^S - \epsilon_U^S - \Sigma_{\sigma}^{\text{ld},r/a}(w) - \bar{\Sigma}^{\text{cor},r/a}(w)}, \quad (40a)$$

$$G_{\sigma}^{S,\leq}(w) = G_{\sigma}^{S,r}(w)[\Sigma_{\sigma}^{\text{ld},\leq}(w) + \bar{\Sigma}^{\text{cor},\leq}(w)]G_{\sigma}^{S,a}(w), \quad (40b)$$

where $\epsilon_U^S = \epsilon_d + Un^S/2$. Here, ϵ_U^S is iterated during the spectral calculation while $h_{\Lambda}^T = h + \tilde{\Lambda}m^T/2$ is taken from the thermodynamic calculation of the two-particle vertex. In such a way the magnetic response remains qualitatively unchanged in the spectral calculations. We stress again that the physical and measurable quantities are determined from the spectral calculations that include the dynamic correlations.

We present in Fig. 4 a flowchart of our two schemes of calculating thermodynamic and spectral quantities. One starts with the initial guess of the thermodynamic charge density n^T , magnetization m^T , and the (irreducible) vertex function $\tilde{\Lambda}$, as

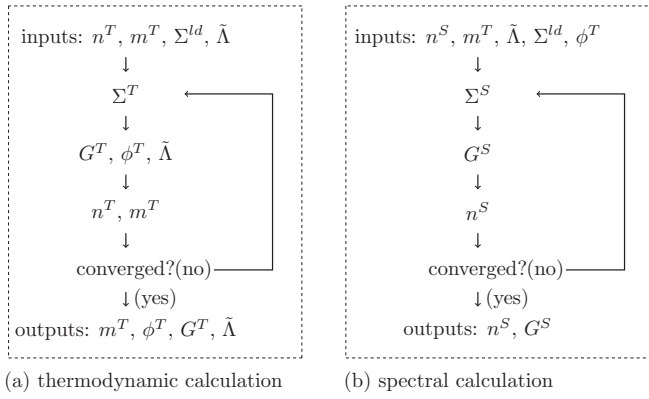


FIG. 4. Flowchart of (a) thermodynamic and (b) spectral calculations.

well as the precalculated lead self-energy Σ^{ld} (by default, Σ^{ld} refers to all the real-time components). With these quantities, we calculate Σ^T and G^T from Eq. (37). The electron-hole bubble ϕ^T and the vertex function $\tilde{\Lambda}$ are then calculated from Eqs. (28)–(31) with G^T . With the newly calculated G^T , we update n^T and m^T , and repeat the above iteration process until convergence is reached for all quantities. After the thermodynamic calculation, we proceed to dynamical corrections to the static mean field by evaluating Σ^S and G^S from the Schwinger-Dyson equation (32) and the Dyson equation (34), respectively. The spectral charge density n^S is then updated from G^S and it is iterated until the iterations converge. Notice that the quantities in the odd sector of the spectral calculation acquire their values from the thermodynamic calculation in order to make magnetic response qualitatively unchanged.

V. RESULTS AND DISCUSSIONS

The reduced parquet equations can be solved in full generality only numerically. However, they can be solved analytically in the Kondo strong-coupling limit at half-filling where the equilibrium solution approaches a critical point. We start with this limit before we analyze the general situation of the steady-state current.

A. Logarithmic scaling in the strong-coupling limit

The SIAM at zero temperature and in the electron-hole symmetric case approaches a critical point in the absence of both magnetic field and bias with increasing interaction strength. We can safely suppress all noncritical fluctuations, which allows us to find an analytic representations of the vanishing Kondo scale. The screening integral (29) can be simplified in this regime to (see Appendix D)

$$R = -\frac{\tilde{\Lambda}^2}{\pi} \int_{-\infty}^0 \text{Im} \frac{[\phi^r(x)]^3}{1 + \tilde{\Lambda}\phi^r(x)} dx, \quad (41)$$

where we used the fluctuation dissipation theorem.

We denote the denominator of the integrand in the screening integral $D^r(x) = 1 + \tilde{\Lambda}\phi^r(x)$. Its static value $D^r(0)$ determines the dimensionless Kondo scale $a_K = D^r(0) = 1 + \tilde{\Lambda}\phi^r(0)$ and vanishes at the critical point. It is proportional to the inverse susceptibility [see Eq. (38)]. An

alternative one-particle spectral definition uses the half-width at half-maximum (HWHM) of the Kondo-Abrikosov-Suhl quasiparticle peak. The advantage of our thermodynamic definition is that it can be determined analytically.

To obtain the Kondo scale, we first expand the denominator function $D^r(x) \approx a_K + \dot{D}^r(0)x$ in small frequencies and keep only the first term that is dominant in the critical region with $a_K \rightarrow 0$. The overdot refers to first-order derivative with respect to frequency. The derivative $\dot{D}^r(0)$ is generally a complex number that at half-filling and without magnetic field becomes purely imaginary. One can explicitly evaluate the real and imaginary parts of $\dot{D}^r(0)$ at zero temperature:

$$\text{Re}\dot{D}^r(0) = \frac{\tilde{\Lambda}}{\pi} \int_{-\infty}^0 dx [\text{Re}\dot{G}^r(x)\text{Im}\tilde{G}^r(x) - \text{Re}\tilde{G}^r(x)\text{Im}\dot{G}^r(x)], \quad (42a)$$

$$\text{Im}\dot{D}^r(0) = -\frac{\tilde{\Lambda}}{\pi} \text{Im}\tilde{G}^r(0)\text{Im}\dot{G}^r(0). \quad (42b)$$

We obtain by putting the above representations into the screening integral and taking into account Eq. (28):

$$\tilde{\Lambda} = \frac{Un^2}{n^2 - 4\tilde{\Lambda}^2[\phi^r(0)]^3 \frac{\text{Im}\dot{D}^r(0)}{|\dot{D}^r(0)|^2} \ln a_K}. \quad (43)$$

By realizing that in the Kondo strong-coupling regime $\tilde{\Lambda} = -1/\phi^r(0)$, $n = 1$, and $\text{Re}\dot{D}^r(0) = 0$, we resolve the above equation and obtain $\ln a_K = \text{Im}\dot{D}^r(0)[1 + \phi^r(0)U]/[4\phi^r(0)]$. Since in the Kondo regime, $U \gg 1$, and we get the explicit analytic solution for the Kondo scale

$$\ln a_K = \frac{U}{4} \text{Im}\dot{D}^r(0). \quad (44)$$

Since the electron-hole bubble is evaluated from the thermodynamic propagators, $\text{Im}\dot{D}^r(0) = 1/(\Gamma)^2$, $\tilde{\Lambda} = \Gamma\pi$ when $U \rightarrow \infty$ and hence $\ln a_K = -U/(4\Gamma)$, which thereby reproduced the linear logarithmic scaling of a_K with the increase of U [2]. The nonuniversal prefactor $1/4$ in our theory slightly differs from $\pi/8$ of the exact solution from the Bethe ansatz [2]. We stress, however, that the scaling coefficient depends on the averaging scheme used in the reduced parquet equations as well as on the density of states on the dot.

B. I-V characteristics in Coulomb-blockade regime

We now turn to the Coulomb-blockade regime to calculate the current-voltage (I-V) characteristics of the steady state. We choose $U = 40\Gamma$ and $T = 0.1\Gamma$. The corresponding Kondo temperature can be estimated by Haldane's formula [63]

$$T_K \approx \frac{\sqrt{2\Gamma U}}{2} \exp \frac{\pi\epsilon_d(\epsilon_d + U)}{2\Gamma U}. \quad (45)$$

The value of the Kondo temperature with our parameters is $T_K \approx 10^{-6}\Gamma$ that is much smaller than the real temperature $T = 0.1\Gamma$ and can be safely neglected. We compare the solution obtained from the reduced parquet equation (RPE) with the Hartree-Fock (HF) mean-field solution that is free of dynamical correlations and also a widely used GW approximation, where the dynamical correlations are added via

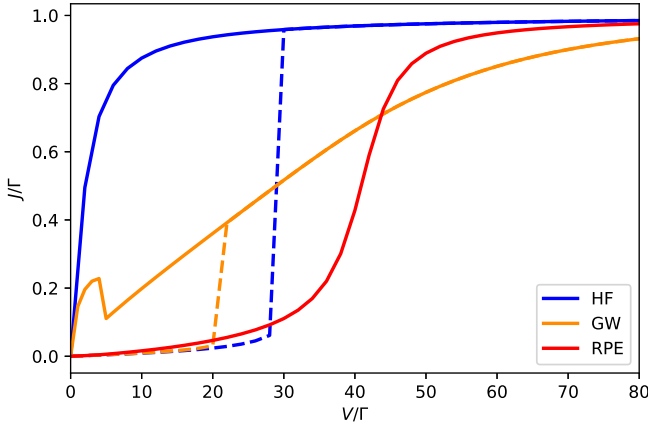


FIG. 5. I-V characteristic curve of the SIAM at half-filling for $U = 40\Gamma$ and $T = 0.1\Gamma$ in the Coulomb-blockade regime calculated by the Hartree-Fock (HF) mean-field, GW approximation, and the reduced parquet equations (RPE). Unphysical hysteresis loop appears in the HF and GW approximations with the solid line corresponding to the nonmagnetic solution and the dashed line to the magnetic one. The RPE suppresses the spurious magnetic order, hence is free of the hysteresis.

the nonlocal screening effect due to the electron-hole pairing [25,64]. We plotted in Fig. 5 the I-V characteristic curve calculated by the HF (blue line), the self-consistent GW (orange line), and the RPE (red line), respectively. Both magnetic (dashed line) and nonmagnetic (solid line) solutions coexist in HF for $V < 30\Gamma$. The current in the nonmagnetic state starts to grow rapidly up to saturation at a larger value of the voltage bias while the current in the magnetic state is strongly suppressed for small biases up to a (spurious) first-order transition to a nonmagnetic state at a threshold value around $V = 30\Gamma$. The magnetic solution in the GW approximation behaves similarly to the HF one where the unphysical magnetic solution is not suppressed and the magnetic solution exists for $V < 22\Gamma$. The rapid growth of the nonmagnetic curve is, however, interrupted with a small hump followed by a less steep increase towards saturation. The current in the RPE follows for weak biases the magnetic solution of the other approximations. The RPE solution leads only to a nonmagnetic state where the spurious magnetic transition with a discrete jump is suppressed. Instead, it continuously crosses over to saturation as determined numerically and experimentally [65,66].

The behaviors of the current in the various approximations can be explained from the corresponding spectral functions displayed in Fig. 6. The step increase of the current with the increasing bias of nonmagnetic HF and GW solutions is caused by a central peak at the Fermi level, which is insensible to a weak applied voltage. The magnetic solution, where the spin-up and -down spectra are split, has small density of states near the Fermi level. There are hence only few electrons to participate in the current. The magnetic solution ceases to exist at larger values of the bias and the transition to the nonmagnetic state leads to a jump in the current.

The RPE solution is nonmagnetic for any bias. There is no central peak in the spectral function for $T \gg T_K$. It contains

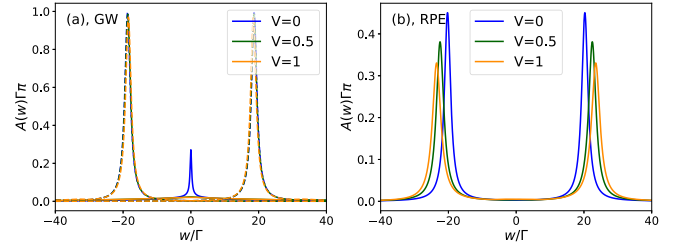


FIG. 6. Spectral function for various voltage biases in GW (left panel) and the reduced parquet equations (right panel) of the SIAM at half-filling, $U = 40\Gamma$, and $T = 0.1\Gamma \gg T_K$. The dashed line corresponds to the magnetic solution while the solid line for the nonmagnetic one.

two Hubbard satellite bands, sitting around $\pm U/2$ away from the Fermi level. With the increasing bias, these two satellite bands do not move too much, and this leads to the S-shape I-V characteristics [65]. In particular, when $V \ll U$, the current is largely suppressed due to the small density of states around the Fermi level, exhibiting a strong Coulomb-blockade effect. The satellite bands start to contribute when the voltage becomes of the order of the position of the satellite Hubbard bands. The RPE result fits well with the magnetic solution of HF and GW at small- V region, due to the similar structure of the spectral functions; however, the magnetic solution breaks the spin symmetry which is unphysical. If we further increase V , the I-V curve will become flat again due to the decay of the density of states at large frequencies.

The stability of the nonmagnetic solution of the RPE is demonstrated on the positivity of the magnetic susceptibility (38), plotted in Fig. 7(a). It is achieved by the two-particle self-consistency in the equation for the effective interaction (28). The interaction is strongly screened for small biases [see Fig. 7(b)]. The voltage suppresses the interaction-induced dynamical fluctuations and the screening of the interaction. Consequently, vertex $\tilde{\Lambda}$ approaches the bare interaction and the susceptibility exponentially decreases with increasing the bias voltage V . The susceptibility remains positive in the whole range of the bias voltage as expected [67].

Furthermore, to quantitatively compare our method with the other existing results, we plot the I-V characteristics for

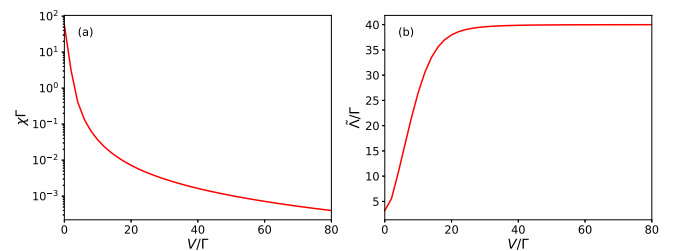


FIG. 7. Magnetic susceptibility (left panel) and the effective interaction $\tilde{\Lambda}$ (right panel) of the SIAM at half-filling, $U = 40\Gamma$, and $T = 0.1\Gamma$ as a function of the voltage bias. The susceptibility is positive and decreases with the bias while the effective interaction increases towards the bare interaction indicating that the bias suppresses the interaction-induced dynamical fluctuations.

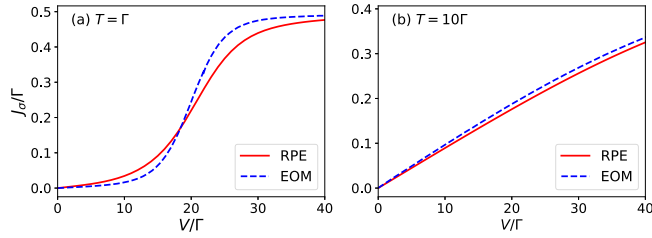


FIG. 8. I-V characteristics at half-filling for $U = 20\Gamma$, (a) $T = \Gamma$ and (b) $T = 10\Gamma$, respectively. Data of EOM are taken from Fig. 3 in Ref. [65].

$U = 20\Gamma$, $T = \Gamma$, and $T = 10\Gamma$ in Figs. 8(a) and 8(b), respectively. The red solid line is our RPE results and the blue dashed line is calculated from the equation-of-motion (EOM) method which read from Fig. 3 in Ref. [65]. The discrepancy of these two methods becomes smaller with the increase of temperature. Note that EOM method, as known, is only valid for Coulomb-blockade regime, namely $T \gg T_K$; however, our RPE method qualitatively captures both Coulomb-blockade and Kondo regimes, which will be discussed in the next subsection.

C. Interplay between Kondo and Coulomb-blockade regimes

We now turn to study the interplay between the Kondo and Coulomb-blockade effects with reduced parquet equations. Both the temperature and the biased voltage should be kept sufficiently low compared with the Kondo temperature T_K to stay inside the Kondo regime. Specifically, for the case we study below, we choose $U = 5\Gamma$ with $T_K \approx 0.222\Gamma$ as estimated from Eq. (45).

Figure 9(a) plots the differential conductance as a function of temperature at zero bias and Fig. 9(b) as a function of voltage bias at zero temperature. We denoted $G_0 = 2e^2/h = 1/\pi$ (in atomic units) the elementary quantum conductance. One can observe three transport regimes with the increase of the temperature: Kondo resonance, cotunneling, and sequential tunneling [22,47]. The zero-bias conductance [Fig. 9(a)] becomes unity at zero temperature due to the Kondo resonance tunneling [46]. It remains in the Kondo regime up to the Kondo temperature T_K where thermal fluctuations start pushing the electrons away from the Fermi energy which leads to a sharp drop of the conductance. When $T_K < T < \Gamma$, the system is driven to the cotunneling regime where the Kondo

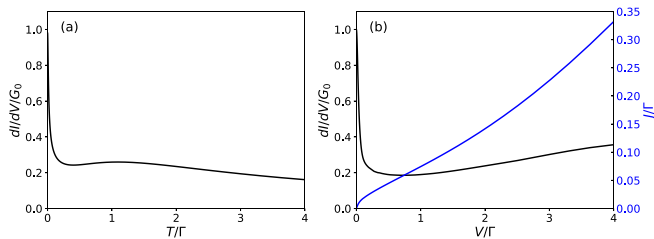


FIG. 9. Differential conductance (black line) of the SIAM at half-filling as a function of temperature in (a) linear response regime $V = 0$ and (b) as a function of voltage far from equilibrium $T = 0$. The blue line in the right panel refers to the current.

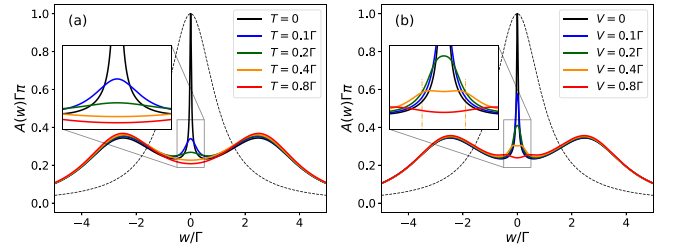


FIG. 10. The spectral function of the SIAM at half-filling and for $U = 5\Gamma$ at different temperatures and zero bias (a) and different voltage biases and zero temperature (b). The thin dashed line is for $U = 0$ at zero-temperature equilibrium state. The vertical lines in the inset of (b) refer to the local chemical potentials of the leads.

peak is effectively suppressed; however, the temperature is not high enough to destroy coherence in the electron system. In this regime, the conductance slightly increases since the Hubbard satellite bands contribute to the effective transport energy window. After T crosses Γ , thermal fluctuations start dominating the system and sequential tunneling plays the major role and the electrons on the QD can be assumed in equilibrium. For this reason, the conductance will finally decrease to zero in the high-temperature limit. When we fix the temperature to be zero and increase the voltage V , the current grows monotonically as shown by the blue curve in Fig. 9(b). Simultaneously, the differential conductance quickly drops for $V < T_K$ in the Kondo regime but starts growing in the cotunneling regime when the voltage becomes sufficiently large [46,68]. Notice that the system does not go through the sequential tunneling regime since there are no thermal fluctuations that would destroy coherence of the transport process.

The behavior of the differential conductance in different regimes can be best understood from the spectral function plotted in Fig. 10 for various temperatures at zero bias, left pane, and various biases at zero temperature, right pane. The spectral function exhibits a typical three-peak structure with the central narrow quasiparticle peak and the satellite Hubbard bands for $T < T_K$ and $V < T_K$. By comparing Figs. 10(a) and 10(b), we see that temperature and voltage bias affect similarly the spectral function by broadening the Kondo resonant peak. With the increase of either T or V to T_K , the central peak is rapidly suppressed with almost intact satellite bands. Aside from that, unlike the temperature-dependent spectral function, the voltage bias further develops local peaks around the chemical potential of each lead. These local peaks are finally destroyed when further increasing the bias, which agrees with the previous experimental results as well as the theoretical studies [10,68,69]. One may further quantitatively compare the nonequilibrium spectral functions in Fig. 10(b) with Fig. 13 in Ref. [69]. One can see that the width of the Kondo peak calculated by RPE is slightly narrower than the numerically exact results at equilibrium and the extra weight of the spectral function is redistributed towards the Hubbard bands. Such a trend is also reported in Fig. 5 of Ref. [42]. With the increase of the bias V , the central peak is suppressed more quickly than in the QMC simulations of Ref. [69]. For example, when $V = 0.8\Gamma$, the Kondo peak from RPE has already been destroyed [red curve in Fig. 10(b)], while it

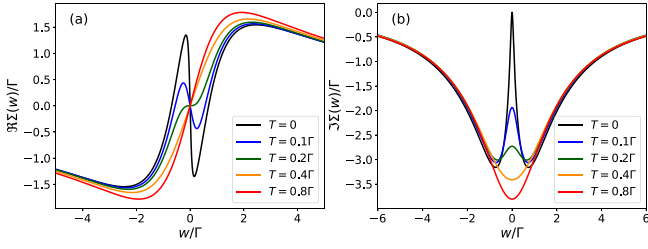


FIG. 11. Real and imaginary parts of the spectral self-energy for various temperatures at equilibrium, corresponding to the spectral function plotted in Fig. 10(a).

just becomes broadened in the QMC result (orange curve in Fig. 13 of Ref. [69]).

The width of the central peak determines a region within which the system behaves as Fermi liquid. This can be seen from the behavior of the self-energy, plotted for various temperatures in Fig. 11. The bias-dependent self-energy has a similar behavior. At zero temperature and zero bias, the real part of the self-energy has a sharp negative slope and the imaginary part vanishes at the Fermi energy. Increasing either temperature or bias, the slope of the real part decreases and the imaginary part becomes increasingly negative. Finally, when the slope of the real part of the self-energy turns positive and the local maximum of the imaginary part turns minimum, the Kondo regime is fully destroyed.

Additionally, we make a quantitative comparison with fRG in the Kondo regime of the I-V characteristics for different interaction strengths in Fig. 12. The solid and dashed-dotted lines are the RPE and fRG, respectively. The fRG data are taken from Fig. 2 in Ref. [70]. The inset in Fig. 12 gives the zoomed-in details around the coordinate origin. For $V < T_K$, the system is in the Kondo regime with a rapid growth of the current, which starts to slow down when V crosses T_K . The discrepancy between these two methods is small when $U = 2$ and becomes larger with the increase of U as shown. In all the cases, the RPE quantitatively underestimate the current compared to the fRG in the Kondo regime. This can

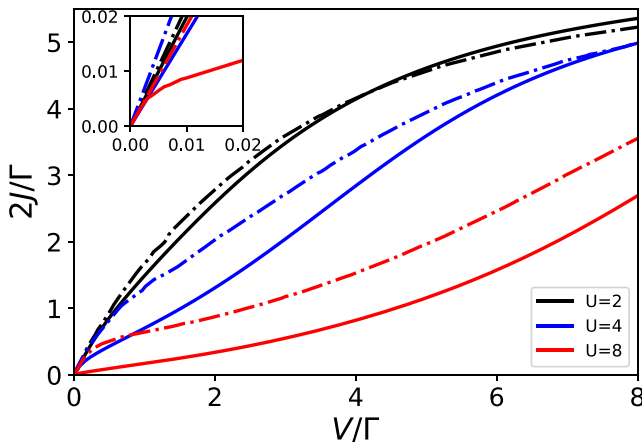


FIG. 12. I-V characteristics for different U at half-filling. Inset: zoomed-in image. Solid lines for RPE and dashed-dotted lines for fRG taken from Fig. 2 of Ref. [70].

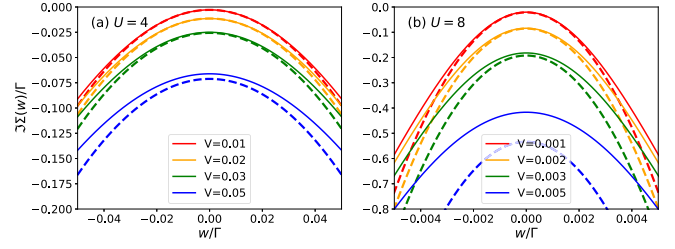


FIG. 13. Imaginary part of the spectral self-energy for various biased voltages ($T = 0$). The solid and dashed lines refer to the results calculated from RPE and Fermi-liquid theory (see Ref. [35]), respectively.

be explained by the behavior of the nonequilibrium spectral function as already discussed [see Fig. 10(b)]. At equilibrium, the central peak evaluated from RPE is narrower than that from the advanced numerical methods. With the increase of V , the Kondo peak quickly vanishes in our RPE method and splits for larger U . The actual current is thus underestimated due to the missing density of states assist of the electrons transported through the dot for low bias.

We further compare the self-energy calculated from the RPE with the one predicted by the Fermi-liquid theory of Ref. [35] in Fig. 13. We plotted its imaginary part for various biased voltages at zero temperature and two interaction strengths. The solid and dashed lines refer to the RPE and the Fermi-liquid theory, respectively. The parameters (spin and charge susceptibilities) of Eq. (20) in Ref. [35] are obtained by fitting the spectral self-energy at zero-temperature equilibrium around the Fermi level. One can see that for relatively low bias, the self-energies from RPE calculation agree quite nicely with the Fermi-liquid results around the Fermi level. The difference between these two methods becomes larger with the increase of V as expected since the voltage destroys the Fermi-liquid state around the zero frequency. Thus, we see that our RPE is qualitatively consistent with the nonequilibrium Fermi-liquid theory.

Finally, we also calculated and compared the conductance as a function of the charging energy U in both the linear response regime and the fully nonequilibrium solution, plotted in Figs. 14(a) and 14(b), respectively. The conductance in the two extreme cases behaves similarly. There is a unity conductance plateau in weak coupling due to the Kondo resonance tunneling [46]. The effective Kondo temperature T_K decreases

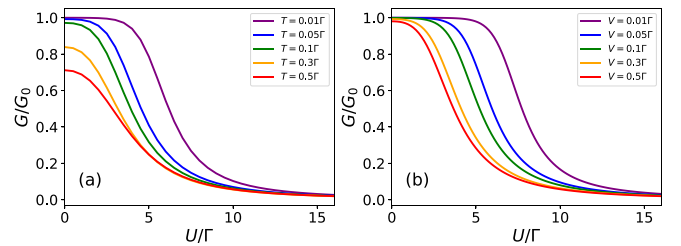


FIG. 14. Conductance as a function of the onsite Coulomb repulsion U for various voltage biases V . Linear response (weak nonequilibrium) regime (left panel) and full nonequilibrium solution (right panel).

with the increasing electron repulsion U and, once its value becomes comparable with T or V , the conductance starts abating with progressive destruction of the Kondo peak. The conductance is significantly suppressed in the extreme limit $U \gg T_K$ due to the Coulomb blockade.

VI. CONCLUSIONS

We extended a two-particle semianalytic approach with the reduced parquet equations and an effective-interaction approximation to an out-of-equilibrium single-impurity Anderson model coupled to two biased metallic leads. The theory was formulated in the critical region of the strong-coupling Kondo limit, capturing the dominant contributions from the spin-flip fluctuations in the instantaneous screened-interaction approximation. It self-consistently determines thermodynamic and spectral quantities. The reduced parquet equations become analytically solvable and reproduce the logarithmic Kondo scaling in the strong-coupling limit. Numerical solutions are used beyond the Kondo critical regime. We reached a qualitative agreement with experimental and more demanding advanced computational techniques. Specifically, the hysteresis loop in the current-voltage characteristics, caused by the spurious phase transition weak-coupling approximations, is fully suppressed in the deep Coulomb-blockade regime, $T \gg T_K$ or $V \gg T_K$, due to the renormalization of the effective interaction. We reproduced qualitatively well the temperature dependence of the zero-bias conductance with three stages: Kondo resonant tunneling $T < T_K$, cotunneling $T_K < T < \Gamma$, and sequential tunneling $T > \Gamma$. If one keeps temperature zero and turns on the bias, the system will experience a crossover from the Kondo resonant regime when $V < T_K$ to a cotunneling regime when $V > T_K$. We proved that the biased voltage plays a similar role as temperature in that they both lead to destroying the central Kondo peak when its value crosses the Kondo temperature T_K . Additionally, the applied voltage also tends to develop peaks around the local chemical potentials in low bias.

The theory proved reliable in the electron-hole symmetric case with the qualitatively correct results for the whole range of the model parameters. Some modifications have to be done to extend consistently the present theory to arbitrary filling, away from the Kondo critical region, to keep the compressibility positive.

ACKNOWLEDGMENT

This work was supported by Grant No. 19-13525S of the Czech Science Foundation.

APPENDIX A: REAL-TIME GREEN FUNCTIONS

Physical quantities are directly related to real-time Green functions. They can be derived from the Keldysh Green function depending on which branch the real-time temporal arguments lie. One defines the following four real-time Green functions [23]:

$$G_{\sigma}^t(t, t') = -i\langle T_t \{d_{\sigma}(t), d_{\sigma}^{\dagger}(t')\} \rangle, \quad (\text{A1})$$

$$G_{\sigma}^<(t, t') = +i\langle d_{\sigma}^{\dagger}(t')d_{\sigma}(t) \rangle, \quad (\text{A2})$$

$$G_{\sigma}^>(t, t') = -i\langle d_{\sigma}(t)d_{\sigma}^{\dagger}(t') \rangle, \quad (\text{A3})$$

$$G_{\sigma}^{\bar{t}}(t, t') = -i\langle T_{\bar{t}} \{d_{\sigma}(t), d_{\sigma}^{\dagger}(t')\} \rangle, \quad (\text{A4})$$

corresponding to (t, t') sitting on $(-, -)$, $(-, +)$, $(+, -)$, and $(+, +)$ branches, respectively. (We used $-$ for the forward branch and $+$ for the backward branch.) Since the above Green functions are linearly dependent, for further ease of use, we introduce another three linearly independent real-time Green functions:

$$G_{\sigma}^r(t, t') = -i\theta(t - t')\langle \{d_{\sigma}(t), d_{\sigma}^{\dagger}(t')\} \rangle, \quad (\text{A5})$$

$$G_{\sigma}^a(t, t') = +i\theta(t' - t)\langle \{d_{\sigma}(t), d_{\sigma}^{\dagger}(t')\} \rangle, \quad (\text{A6})$$

$$G_{\sigma}^k(t, t') = -i\langle [d_{\sigma}(t), d_{\sigma}^{\dagger}(t')] \rangle. \quad (\text{A7})$$

In the above formulas we denoted $\{A, B\} = AB + BA$ and $[A, B] = AB - BA$ the anticommutator and commutator, respectively. As a result, G_{σ}^t , $G_{\sigma}^<$, $G_{\sigma}^>$, and $G_{\sigma}^{\bar{t}}$ can be expressed as a linear combination of G_{σ}^r , G_{σ}^a , and G_{σ}^k via [71]

$$\begin{bmatrix} G_{\sigma}^t & -G_{\sigma}^< \\ G_{\sigma}^> & -G_{\sigma}^{\bar{t}} \end{bmatrix} = \frac{1}{2} \begin{bmatrix} G_{\sigma}^r + G_{\sigma}^a + G_{\sigma}^k & G_{\sigma}^r - G_{\sigma}^a - G_{\sigma}^k \\ G_{\sigma}^r - G_{\sigma}^a + G_{\sigma}^k & G_{\sigma}^r + G_{\sigma}^a - G_{\sigma}^k \end{bmatrix}, \quad (\text{A8})$$

where we used identities $G_{\sigma}^> + G_{\sigma}^< = G_{\sigma}^r + G_{\sigma}^{\bar{t}}$ and $G_{\sigma}^r - G_{\sigma}^a = G_{\sigma}^> - G_{\sigma}^<$. One can similarly define the bosonic Green functions with the proper change of the quantum statistics. They satisfy the same relations defined above.

APPENDIX B: LEAD SELF-ENERGY

The self-energy of the s lead can formally be written as

$$\Sigma_{s\sigma}^{\text{ld}}(z_1, z_2) = \sum_k t_{sk} t_{sk}^* G_{s,kk,\sigma}^{cc,0}(z_1, z_2), \quad (\text{B1})$$

where

$$G_{s,kk',\sigma}^{cc,0}(z_1, z_2) = -i\langle T_{\triangleright} \{c_{sk\sigma}(z_1), c_{s k'\sigma}^{\dagger}(z_2)\} \rangle_0 \quad (\text{B2})$$

is the decoupled c -electron Keldysh Green function. (The subscript “0” implies that the average is taken over the lead Hamiltonian only.) Since the lead is assumed to be in local equilibrium and in the frequency domain, we have

$$G_{s,kk,\sigma}^{cc,0,r}(w) = \frac{1}{w - \epsilon_{sk\sigma} + \mu_s + i\eta}. \quad (\text{B3})$$

Therefore, the self-energy of the s lead becomes

$$\Sigma_{s\sigma}^{\text{ld},r}(w) = \frac{1}{\pi} \int_{-\infty}^{\infty} dx \frac{\Gamma_{s\sigma}(x)}{w - x + i\eta}, \quad (\text{B4})$$

where $\Gamma_{s\sigma}(x) = \pi \rho_{s\sigma}(x) t_{sk}(x) t_{sk}^*(x)$ is the linewidth function and $\rho_{s\sigma}(x) = \sum_k \delta(x - \epsilon_{sk\sigma} + \mu_s)$ is the spin-resolved density of states of the s lead.

In wide-band limit (WBL), we assume $\Gamma_{s\sigma}(x) = \Gamma_{s\sigma} \theta(|x - \mu_s| < D)$ where $\theta(x)$ is the Heaviside step function. The s -lead self-energy then is

$$\Sigma_{s\sigma}^{\text{ld},r}(w) = \frac{\Gamma_{s\sigma}}{\pi} \ln \left| \frac{D + (w - \mu_s)}{D - (w - \mu_s)} \right| - i\Gamma_{s\sigma} \theta(|w - \mu_s| < D). \quad (\text{B5})$$

We further set $D \rightarrow \infty$, $\Sigma_{s\sigma}^{\text{ld},r}(w) = -i\Gamma_{s\sigma}$. The lesser and greater s -lead self-energies can be obtained by fluctuation dissipation theorem [23]

$$\Sigma_{s\sigma}^{\text{ld},<}(w) = -2if_s(w)\text{Im}\Sigma_{s\sigma}^{\text{ld},r}(w), \quad (\text{B6})$$

$$\Sigma_{s\sigma}^{\text{ld},>}(w) = 2i[1 - f_s(w)]\text{Im}\Sigma_{s\sigma}^{\text{ld},r}(w), \quad (\text{B7})$$

where $f_s(w) = 1/(e^{\beta(w-\mu_s)} + 1)$ is the Fermi-Dirac distribution function.

APPENDIX C: DERIVATION OF EQ. (29)

We start from Eq. (25). The complex variable z in $R(z)$ can be chosen either on the forward or backward branch, which is irrelevant to the final result. By applying the Langreth's rules [23] we obtain

$$\begin{aligned} R^-(t) = & i \int_{-\infty}^{\infty} dt_1 dt_2 [\phi^t(t, t_1) \tilde{\mathcal{K}}^t(t_1, t_2) \phi^t(t_2, t) \\ & - \phi^t(t, t_1) \tilde{\mathcal{K}}^<(t_1, t_2) \phi^>(t_2, t) \\ & - \phi^<(t, t_1) \tilde{\mathcal{K}}^>(t_1, t_2) \phi^a(t_2, t) \\ & - \phi^<(t, t_1) \tilde{\mathcal{K}}^r(t_1, t_2) \phi^>(t_2, t)], \end{aligned} \quad (\text{C1})$$

$$\begin{aligned} R^+(t) = & i \int_{-\infty}^{\infty} dt_1 dt_2 [\phi^>(t, t_1) \tilde{\mathcal{K}}^<(t_1, t_2) \phi^a(t_2, t) \\ & + \phi^>(t, t_1) \tilde{\mathcal{K}}^r(t_1, t_2) \phi^<(t_2, t) \\ & - \phi^{\bar{t}}(t, t_1) \tilde{\mathcal{K}}^>(t_1, t_2) \phi^<(t_2, t) \\ & + \phi^{\bar{t}}(t, t_1) \tilde{\mathcal{K}}^{\bar{t}}(t_1, t_2) \phi^{\bar{t}}(t_2, t)], \end{aligned} \quad (\text{C2})$$

where superscript “-” (“+”) refers to t lying on the forward (backward) branch. By considering the relations between the real-time Green functions given in Eq. (A8), after averaging R^- and R^+ followed by the Fourier transform, one obtains Eq. (29).

APPENDIX D: FORMULAS AT EQUILIBRIUM

In equilibrium, the above-formulated equations can be simplified by applying the fluctuation-dissipation theorem [23] which imposes an additional relation between lesser or greater quantities and the corresponding spectral functions. Specifically, the renormalization integral in Eq. (29) only depends on the retarded components, that is,

$$R = -\frac{1}{2\pi} \mathcal{P} \int_{-\infty}^{\infty} dx [1 + 2b(x)] \{2 \text{Im}\phi^r(x) \text{Re}\mathcal{K}^r(x) \text{Re}\phi^r(x) - [\text{Im}\phi^r(x)]^2 \text{Im}\mathcal{K}^r(x) + \text{Im}\mathcal{K}^r(x) [\text{Re}\phi^r(x)]^2\}, \quad (\text{D1})$$

where $\mathcal{P} \int dx$ refers to the principal-value integral and $b(x)$ is the Bose-Einstein distribution function. By considering the symmetry relation $X^{r/a}(x) = X^{a/r}(-x)$ ($X \in \{\mathcal{K}, \phi\}$), each term in the second brackets is an odd function with respect to x so that only when they are multiplied by $b(x)$ they contribute. As a result,

$$R = -\frac{1}{\pi} \mathcal{P} \int_{-\infty}^{\infty} b(x) \text{Im}[\phi^r(x) \mathcal{K}^r(x) \phi^r(x)] dx = \frac{\tilde{\Lambda}^2}{\pi} \mathcal{P} \int_{-\infty}^{\infty} b(x) \text{Im} \frac{[\phi^r(x)]^3}{1 + \tilde{\Lambda} \phi^r(x)} dx, \quad (\text{D2})$$

where we used $\tilde{\mathcal{K}}^r(x) = -\tilde{\Lambda}^2 \frac{\phi^r(x)}{1 + \tilde{\Lambda} \phi^r(x)}$. Similarly, the equilibrium formula for the even self-energy, Eq. (32a), is given by $\tilde{\Sigma}^{\text{int},r}(w) = \frac{U\tilde{n}}{2} + \tilde{\Sigma}^{\text{cor},r}(w)$, where

$$\tilde{\Sigma}^{\text{cor},r}(w) = -\frac{U\tilde{\Lambda}}{2\pi} \sum_{\sigma} \mathcal{P} \int_{-\infty}^{\infty} dx \left[b(x) \text{Im} \frac{\phi^r(x)}{1 + \tilde{\Lambda} \phi^r(x)} \tilde{G}^r(w-x) - f(x) \frac{\phi^r(x+w)}{1 + \tilde{\Lambda} \phi^r(x+w)} \text{Im} \tilde{G}^a(-x) \right], \quad (\text{D3})$$

and the odd self-energy, Eq. (33a), is unchanged, i.e., $\Delta\Sigma^r(w) = -\frac{m}{2}\tilde{\Lambda}$. The calculation of the electron-hole bubble at equilibrium is simplified to

$$\phi^r(w) = -\frac{1}{\pi} \int_{-\infty}^{\infty} dx f(x) [\tilde{G}^a(x-w) \text{Im} \tilde{G}^r(x) + \tilde{G}^r(x+w) \text{Im} \tilde{G}^r(x)], \quad (\text{D4})$$

and at zero frequency, it reads as

$$\phi^r(0) = -\frac{1}{\pi} \int_{-\infty}^{\infty} dx f(x) \text{Im}[\tilde{G}^r(x) \tilde{G}^r(x)]. \quad (\text{D5})$$

- [1] P. W. Anderson, Localized magnetic states in metals, *Phys. Rev.* **124**, 41 (1961).
 [2] A. C. Hewson, *The Kondo Problem to Heavy Fermions*, Vol. 2 (Cambridge University Press, Cambridge, 1997)
 [3] V. Janiš, A. Klíč, J. Yan, and V. Pokorný, Curie-Weiss susceptibility in strongly correlated electron systems, *Phys. Rev. B* **102**, 205120 (2020).

- [4] A. Tsvetick and P. Wiegmann, Exact results in the theory of magnetic alloys, *Adv. Phys.* **32**, 453 (1983).
 [5] A. Georges, G. Kotliar, W. Krauth, and M. J. Rozenberg, Dynamical mean-field theory of strongly correlated fermion systems and the limit of infinite dimensions, *Rev. Mod. Phys.* **68**, 13 (1996).

- [6] G. Kotliar, S. Y. Savrasov, K. Haule, V. S. Oudovenko, O. Parcollet, and C. A. Marianetti, Electronic structure calculations with dynamical mean-field theory, *Rev. Mod. Phys.* **78**, 865 (2006); G. Kotliar and D. Vollhardt, Strongly correlated materials: Insights from dynamical mean-field theory, *Phys. Today* **57**(3), 53 (2004).
- [7] V. Meden, The Anderson-Josephson quantum dot—a theory perspective, *J. Phys.: Condens. Matter* **31**, 163001 (2019); B. Josephson, Possible new effects in superconductive tunnelling, *Phys. Lett.* **1**, 251 (1962); M. Žonda, V. Pokorný, V. Janiš, and T. Novotný, Perturbation theory of a superconducting $0 - \pi$ impurity quantum phase transition, *Sci. Rep.* **5**, 8821 (2015).
- [8] N. C. van der Vaart, S. F. Godijn, Y. V. Nazarov, C. J. P. M. Harmans, J. E. Mooij, L. W. Molenkamp, and C. T. Foxon, Resonant Tunneling through Two Discrete Energy States, *Phys. Rev. Lett.* **74**, 4702 (1995); T. Fujisawa, T. H. Oosterkamp, W. G. van der Wiel, B. W. Broer, R. Aguado, S. Tarucha, and L. P. Kouwenhoven, Spontaneous emission spectrum in double quantum dot devices, *Science* **282**, 932 (1998).
- [9] L. Li, M.-X. Gao, Z.-H. Wang, H.-G. Luo, and W.-Q. Chen, Rashba-induced kondo screening of a magnetic impurity in a two-dimensional superconductor, *Phys. Rev. B* **97**, 064519 (2018).
- [10] Y. Meir, N. S. Wingreen, and P. A. Lee, Low-Temperature Transport through a Quantum Dot: The Anderson Model Out of Equilibrium, *Phys. Rev. Lett.* **70**, 2601 (1993).
- [11] T. L. Schmidt, P. Werner, L. Mühlbacher, and A. Komnik, Transient dynamics of the anderson impurity model out of equilibrium, *Phys. Rev. B* **78**, 235110 (2008).
- [12] R. Van Roermund, S.-y. Shiau, and M. Lavagna, Anderson model out of equilibrium: Decoherence effects in transport through a quantum dot, *Phys. Rev. B* **81**, 165115 (2010).
- [13] P. Werner, T. Oka, and A. J. Millis, Diagrammatic monte carlo simulation of nonequilibrium systems, *Phys. Rev. B* **79**, 035320 (2009); P. Werner, T. Oka, M. Eckstein, and A. J. Millis, Weak-coupling quantum Monte Carlo calculations on the Keldysh contour: Theory and application to the current-voltage characteristics of the anderson model, *ibid.* **81**, 035108 (2010).
- [14] J. E. Han, A. Dirks, and T. Pruschke, Imaginary-time quantum many-body theory out of equilibrium: Formal equivalence to keldysh real-time theory and calculation of static properties, *Phys. Rev. B* **86**, 155130 (2012).
- [15] F. B. Anders and A. Schiller, Real-Time Dynamics in Quantum-Impurity Systems: A Time-Dependent Numerical Renormalization-Group Approach, *Phys. Rev. Lett.* **95**, 196801 (2005); F. B. Anders, A numerical renormalization group approach to non-equilibrium Green functions for quantum impurity models, *J. Phys.: Condens. Matter* **20**, 195216 (2008).
- [16] R. Gezzi, T. Pruschke, and V. Meden, Functional renormalization group for nonequilibrium quantum many-body problems, *Phys. Rev. B* **75**, 045324 (2007).
- [17] S. G. Jakobs, V. Meden, and H. Schoeller, Nonequilibrium Functional Renormalization Group for Interacting Quantum Systems, *Phys. Rev. Lett.* **99**, 150603 (2007); S. G. Jakobs, M. Pletyukhov, and H. Schoeller, Nonequilibrium functional renormalization group with frequency-dependent vertex function: A study of the single-impurity anderson model, *Phys. Rev. B* **81**, 195109 (2010).
- [18] A. J. Daley, C. Kollath, U. Schollwöck, and G. Vidal, Time-dependent density-matrix renormalization-group using adaptive effective hilbert spaces, *J. Stat. Mech.: Theory Exp.* (2004) P04005.
- [19] S. R. White and A. E. Feiguin, Real-Time Evolution Using the Density Matrix Renormalization Group, *Phys. Rev. Lett.* **93**, 076401 (2004).
- [20] F. Heidrich-Meisner, A. E. Feiguin, and E. Dagotto, Real-time simulations of nonequilibrium transport in the single-impurity Anderson model, *Phys. Rev. B* **79**, 235336 (2009).
- [21] H.-G. Luo, Z.-J. Ying, and S.-J. Wang, Equation of motion approach to the solution of the Anderson model, *Phys. Rev. B* **59**, 9710 (1999).
- [22] H. Bruus and K. Flensberg, *Many-body Quantum Theory in Condensed Matter Physics: An Introduction* (Oxford University Press, Oxford, 2004).
- [23] H. Haug, A.-P. Jauho, and M. Cardona, *Quantum Kinetics in Transport and Optics of Semiconductors*, Vol. 2 (Springer, Berlin, 2008).
- [24] G. Stefanucci and R. Van Leeuwen, *Nonequilibrium Many-body Theory of Quantum Systems: A Modern Introduction* (Cambridge University Press, Cambridge, 2013).
- [25] K. S. Thygesen and A. Rubio, Conserving gw scheme for nonequilibrium quantum transport in molecular contacts, *Phys. Rev. B* **77**, 115333 (2008); C. D. Spataru, M. S. Hybertsen, S. G. Louie, and A. J. Millis, Gw approach to anderson model out of equilibrium: Coulomb blockade and false hysteresis in the i - v characteristics, *ibid.* **79**, 155110 (2009).
- [26] J. Paaske, A. Rosch, J. Kroha, and P. Wölfle, Nonequilibrium transport through a kondo dot: Decoherence effects, *Phys. Rev. B* **70**, 155301 (2004).
- [27] D. M. Fugger, D. Bauernfeind, M. E. Sorantin, and E. Arrigoni, Nonequilibrium pseudogap anderson impurity model: A master equation tensor network approach, *Phys. Rev. B* **101**, 165132 (2020).
- [28] M. Lotem, A. Weichselbaum, J. von Delft, and M. Goldstein, Renormalized lindblad driving: A numerically exact nonequilibrium quantum impurity solver, *Phys. Rev. Research* **2**, 043052 (2020).
- [29] G. Stefanucci and S. Kurth, Steady-state density functional theory for finite bias conductances, *Nano Lett.* **15**, 8020 (2015). S. Kurth and G. Stefanucci, Nonequilibrium anderson model made simple with density functional theory, *Phys. Rev. B* **94**, 241103(R) (2016).
- [30] D. Jacob and S. Kurth, Many-body spectral functions from steady state density functional theory, *Nano Lett.* **18**, 2086 (2018).
- [31] M. Hopjan, D. Karlsson, S. Ydman, C. Verdozzi, and C.-O. Almbladh, Merging Features from Green's Functions and Time Dependent Density Functional Theory: A Route to the Description of Correlated Materials Out of Equilibrium? *Phys. Rev. Lett.* **116**, 236402 (2016).
- [32] S. Weiss, J. Eckel, M. Thorwart, and R. Egger, Iterative real-time path integral approach to nonequilibrium quantum transport, *Phys. Rev. B* **77**, 195316 (2008).
- [33] D. Bauernfeind, M. Zingl, R. Triebl, M. Aichhorn, and H. G. Evertz, Fork Tensor-Product States: Efficient Multiorbital Real-Time Dmft Solver, *Phys. Rev. X* **7**, 031013 (2017).
- [34] A. Dorda, M. Ganahl, H. G. Evertz, W. von der Linden, and E. Arrigoni, Auxiliary master equation approach within matrix product states: Spectral properties of the nonequilibrium Anderson impurity model, *Phys. Rev. B* **92**, 125145 (2015).

- [35] A. Oguri, Fermi-liquid theory for the Anderson model out of equilibrium, *Phys. Rev. B* **64**, 153305 (2001).
- [36] C. Mora, P. Vitushinsky, X. Leyronas, A. A. Clerk, and K. Le Hur, Theory of nonequilibrium transport in the su(n) Kondo regime, *Phys. Rev. B* **80**, 155322 (2009).
- [37] C. Mora, C. P. Moca, J. von Delft, and G. Zaránd, Fermi-liquid theory for the single-impurity Anderson model, *Phys. Rev. B* **92**, 075120 (2015).
- [38] A. Oguri and A. C. Hewson, Higher-Order Fermi-Liquid Corrections for an Anderson Impurity Away from Half Filling, *Phys. Rev. Lett.* **120**, 126802 (2018).
- [39] V. Janiš and P. Augustinský, Analytic impurity solver with Kondo strong-coupling asymptotics, *Phys. Rev. B* **75**, 165108 (2007); Kondo behavior in the asymmetric Anderson model: Analytic approach, **77**, 085106 (2008).
- [40] V. Janiš, A. Kauch, and V. Pokorný, Thermodynamically consistent description of criticality in models of correlated electrons, *Phys. Rev. B* **95**, 045108 (2017).
- [41] V. Janiš, V. Pokorný, and A. Kauch, Mean-field approximation for thermodynamic and spectral functions of correlated electrons: Strong coupling and arbitrary band filling, *Phys. Rev. B* **95**, 165113 (2017).
- [42] V. Janiš, P. Zalom, V. Pokorný, and A. Klíč, Strongly correlated electrons: Analytic mean-field theories with two-particle self-consistency, *Phys. Rev. B* **100**, 195114 (2019).
- [43] V. Janiš and A. Klíč, Kondo temperature and high to low temperature crossover in impurity models of correlated electrons, *Jpn. Phys. Soc. Conf. Proc.* **30**, 011124 (2020).
- [44] S. M. Cronenwett, T. H. Oosterkamp, and L. P. Kouwenhoven, A tunable Kondo effect in quantum dots, *Science* **281**, 540 (1998).
- [45] D. Goldhaber-Gordon, H. Shtrikman, D. Mahalu, D. Abusch-Magder, U. Meirav, and M. A. Kastner, Kondo effect in a single-electron transistor, *Nature (London)* **391**, 156 (1998).
- [46] W. G. Van der Wiel, S. D. Franceschi, T. Fujisawa, J. M. Elzerman, S. Tarucha, and L. P. Kouwenhoven, The Kondo effect in the unitary limit, *Science* **289**, 2105 (2000).
- [47] M. Pustilnik and L. Glazman, Kondo effect in quantum dots, *J. Phys.: Condens. Matter* **16**, R513 (2004).
- [48] M. Wagner, Expansions of nonequilibrium Green's functions, *Phys. Rev. B* **44**, 6104 (1991).
- [49] J. Schwinger, Brownian motion of a quantum oscillator, *J. Math. Phys.* **2**, 407 (1961).
- [50] L. Keldysh, Diagram technique for nonequilibrium processes, *Sov. Phys. JETP* **20**, 1018 (1965).
- [51] A. Kamenev, *Field Theory of Non-equilibrium Systems* (Cambridge University Press, Cambridge, 2011).
- [52] A.-P. Jauho, N. S. Wingreen, and Y. Meir, Time-dependent transport in interacting and noninteracting resonant-tunneling systems, *Phys. Rev. B* **50**, 5528 (1994).
- [53] G. Baym and L. P. Kadanoff, Conservation laws and correlation functions, *Phys. Rev.* **124**, 287 (1961).
- [54] G. Baym, Self-consistent approximations in many-body systems, *Phys. Rev.* **127**, 1391 (1962).
- [55] L. P. Kadanoff and G. A. Baym, *Quantum Statistical Mechanics* (Benjamin, New York, 1962).
- [56] N. Bickers, Parquet equations for numerical self-consistent-field theory, *Int. J. Mod. Phys. B* **05**, 253 (1991).
- [57] V. Janiš, The Hubbard model at intermediate coupling: renormalization of the interaction strength, *J. Phys.: Condens. Matter* **10**, 2915 (1998).
- [58] V. Janiš, Stability of self-consistent solutions for the Hubbard model at intermediate and strong coupling, *Phys. Rev. B* **60**, 11345 (1999).
- [59] G. Rohringer, H. Hafermann, A. Toschi, A. A. Katanin, A. E. Antipov, M. I. Katsnelson, A. I. Lichtenstein, A. N. Rubtsov, and K. Held, Diagrammatic routes to nonlocal correlations beyond dynamical mean field theory, *Rev. Mod. Phys.* **90**, 025003 (2018).
- [60] V. Janiš, Green functions in the renormalized many-body perturbation theory for correlated and disordered electrons, *Condens. Matter Phys.* **9**, 499 (2006).
- [61] V. Janiš and J. Yan, Many-body perturbation theory for the superconducting quantum dot: Fundamental role of the magnetic field, *Phys. Rev. B* **103**, 235163 (2021).
- [62] V. Janiš, A. Klíč, and J. Yan, Antiferromagnetic fluctuations in the one-dimensional Hubbard model, *AIP Adv.* **10**, 125127 (2020).
- [63] F. D. M. Haldane, Scaling Theory of The Asymmetric Anderson Model, *Phys. Rev. Lett.* **40**, 416 (1978).
- [64] X. Wang, C. D. Spataru, M. S. Hybertsen, and A. J. Millis, Electronic correlation in nanoscale junctions: Comparison of the gw approximation to a numerically exact solution of the single-impurity Anderson model, *Phys. Rev. B* **77**, 045119 (2008).
- [65] A. Levy, L. Kidon, J. Bätge, J. Okamoto, M. Thoss, D. T. Limmer, and E. Rabani, Absence of coulomb blockade in the Anderson impurity model at the symmetric point, *J. Phys. Chem. C* **123**, 13538 (2019).
- [66] G. Zhang, C.-H. Chung, C.-T. Ke, C.-Y. Lin, H. Mebrahtu, A. I. Smirnov, G. Finkelstein, and H. U. Baranger, Nonequilibrium quantum critical steady state: Transport through a dissipative resonant level, *Phys. Rev. Research* **3**, 013136 (2021).
- [67] A. Dirks, S. Schmitt, J. E. Han, F. Anders, P. Werner, and T. Pruschke, Double occupancy and magnetic susceptibility of the Anderson impurity model out of equilibrium, *Europhys. Lett.* **102**, 37011 (2013).
- [68] F. B. Anders, Steady-State Currents through Nanodevices: A Scattering-States Numerical Renormalization-Group Approach to Open Quantum Systems, *Phys. Rev. Lett.* **101**, 066804 (2008).
- [69] C. Bertrand, S. Florens, O. Parcollet, and X. Waintal, Reconstructing Nonequilibrium Regimes of Quantum Many-Body Systems from the Analytical Structure of Perturbative Expansions, *Phys. Rev. X* **9**, 041008 (2019).
- [70] J. Eckel, F. Heidrich-Meisner, S. G. Jakobs, M. Thorwart, M. Pletyukhov, and R. Egger, Comparative study of theoretical methods for non-equilibrium quantum transport, *New J. Phys.* **12**, 043042 (2010).
- [71] J. Yan and Y. Ke, Generalized nonequilibrium vertex correction method in coherent medium theory for quantum transport simulation of disordered nanoelectronics, *Phys. Rev. B* **94**, 045424 (2016); J. Yan, S. Wang, K. Xia, and Y. Ke, First-principles quantum transport method for disordered nanoelectronics: Disorder-averaged transmission, shot noise, and device-to-device variability, *ibid.* **95**, 125428 (2017).